Measuring advection and diffusion of colloids in shear flow

by M.H.G. Duits*, S. Ghosh and F. Mugele

Physics of Complex Fluids group, MESA+ institute, University of Twente
PO Box 217, 7500 AE Enschede, The Netherlands
**Corresponding author, email: M.H.G.Duits@utwente.nl*

ABSTRACT

Analysis of the dynamics of colloids in shear flow can be challenging because of the superposition of diffusion and advection. We present a method that separates the two motions, starting from the time-dependent particle coordinates. Restriction of the tracking to flow lanes and subtraction of estimated advective displacements are combined in an iterative scheme that eventually makes the spatial segmentation redundant. Tracking errors due to neglect of lateral diffusion are avoided, while drifts parallel and perpendicular to the flow are eliminated. After explaining the principles of our method, we validate it against both computer simulations and experiments. A critical overall test is provided by the Mean Square Displacement function at high Peclet numbers (up to 50). We demonstrate via simulations how the measurement accuracy depends on diffusion coefficients and flow rates, expressed in units of camera pixels and frames. Also sample-specific issues are addressed: inaccuracies in the velocity profile for dilute suspensions (Volume Fraction ≤ 0.03), and tracking errors for concentrated ones (VF ≥ 0.3). Analysis of experiments with colloidal spheres flowing through micro channels corroborates these findings, and indicates perspectives for studies on transport, mixing or rheology in microfluidic environments.

Keywords: colloids, particle tracking, diffusion, advection, rheology, microfluidics, microscopy

1. INTRODUCTION

The behavior of colloidal particles in microscopic geometries is of interest for a growing number of applications like their synthesis in droplets [1] or microfluidic channels [2], their use as (bio)sensors in microfluidic chips [3], assembly in confined geometries [4], and transport through capillaries [5, 6] or porous networks [7]. Also from a fundamental point of view these systems are interesting, an important reason being that geometrical confinement can strongly influence both the spatial distribution and the dynamics of the particles [8-12]. The recent emergence of microfluidics has further enhanced this interest by adding shear flow as an additional dimension to the problem. The combination of confinement and spatially varying flow has been addressed at the level of the advective velocity and concentration profiles [5, 6, 13-17]. However data on the diffusive dynamics in flow are scarce, especially for Brownian particles. One reason for this could be the difficulties in analyzing the behavior of particles that show both diffusion and advection.

In the flow of colloidal suspensions, two types of motion are superimposed onto each other. On one hand the particles tend to follow the streamlines of the overall material, but on the other they also deviate from it, due to collisions with either solvent molecules or other particles. From a scientific point of view, both types of motion are of interest. The advective (average) motion as characterized

by the flow profile reflects the nonlinear rheological behavior of the material [18-20]. Knowing the driving force (e.g. a pressure drop) and the geometry (e.g. a capillary or a rectangular channel), the measured velocity profile can be either inverted or fitted to a flow curve (e.g. [18]). The deviatoric (stochastic) motions of the colloids contain complementary information. Depending on the fulfilment of certain assumptions about the probe-matrix interactions, they can reveal local viscoelastic properties of the material surrounding the particles [21-27] .

However the problem is how to separate the two types of motion from each other (in a video microscopy experiment). The stochastic motion adds 'noise' which should be properly 'averaged out' before the advective motion can be found. Conversely, the average motion provides a background signal which has to be subtracted before the fluctuations can be quantified. This problem is not exclusive to colloids; it is also encountered in flow of suspensions of much bigger particles [28-30] and dry granular flows [31], where the diffusion is not Brownian but collision-induced. For non-colloidal particles in a homogeneous shear flow, the diffusive dynamics could be extracted using a correlation technique [29, 30, 32]. More recently also flows with gradients in shear have been considered. Besseling *et al* [33] describe the combination of image correlation and particle tracking to find velocity profiles of concentrated suspensions flowing through micro channels.

In spite of these significant achievements, there are still regimes of relevance for fundamental and applied studies, in which decomposition of the particle motions into advection and diffusion remains challenging. A good example is the case of colloids flowing at high Peclet numbers, where it has been found that concentration gradients can develop as a consequence of shear induced diffusion [5, 6, 34]. However measurements of the diffusion coefficients themselves were not presented for this case. It is clear why these are difficult: the stochastic displacements are relatively very small.

In this paper we present a method that tackles this problem by combining a careful tracking of particle displacements with a precise subtraction of the local advective motion. Tracking erratically moving particles in high speed flow is a well-recognized problem. The standard routine for micro-rheological applications at rest [35] tries to find the new position of each particle in the next video image by searching within a circle. Use of the same method in flow, presents a challenge. In case of directional motion with velocity v detected with a time resolution Δt, the search radius needs to be (at least) $v*\Delta t$. If this radius becomes so large that other particles are found inside the same circle, ambiguities occur, leading to (very detrimental) misidentifications. Clearly one remedy could be to diminish Δt via the speed of the camera. But regardless of the success of the latter, the desire to 'stretch' the range of addressable flow speeds via an improved data analysis will always remain.

One such improvement consists of subtracting the estimated advective displacement prior to the tracking, and applying this in an iterative scheme. This approach has been successfully used but a remaining issue, called 'accumulated strain' was identified for high shear flows [33]. Also other (potential) issues of tracking in high shear flows exist, which have not been addressed sofar. Scarcity of the particles is a notable one, with implications for the study of dilute systems (e.g. use of the colloids as diffusive tracers). In this regime, accurate measurement of the velocity profile requires an experiment of long duration, which in turn can generate (more prominent) issues with fluctuations in the flow or drift of the microscope table. We will present mitigations to each of these issues.

Regarding the measurement of diffusive behavior, it is important to note that (near) absence of particle misidentifications is required but not necessarily sufficient. Even if the tracking is flawless, the mentioned issues with noise or velocity drifts may cause significant inaccuracies in the apparent

diffusive behavior. For this reason we will consider the measured Mean Squared Displacement (MSD) function as the benchmark of our analysis.

After explaining the principles of our method, we will first validate it by comparison to computer simulations in which an isotropic Brownian diffusion is superimposed onto a parabolic flow profile. Tagging of particles is used to quantify the proportion of tracking errors, as a function of particle concentration, flow rate and diffusivity. Additional analysis of the apparent diffusion coefficients a function of these parameters, then allows a certain disentanglement of the contributions of tracking errors and velocity errors to the (in)accuracy of the MSDs. Further, also analysis of experiments in microchannel flow will be presented. Here we will highlight the difference between the analysis at high and low particle concentrations, and demonstrate the effect of corrections for drift.

2. EXPERIMENTS

Rectangular microchannels were fabricated by bonding a PDMS slab containing the side walls and ceiling onto a 170 µm thick glass coverslip. Particle-laden fluids were pumped through by setting a difference in hydrostatic pressure between inlet and outlet (see [36] for details). All suspensions consisted of 1 µm diameter silica spheres with fluorescent cores (see [37, 38] for synthesis and characterization details) dispersed in a refractive-index matching mixture of water and glycerol with a viscosity of ≈100 mPa.s. Fluids were prepared at volume fractions ϕ of 0.03 and 0.3.
All channels (see Fig. 1) had a length of 2 cm, while their (width x height) cross sections were 30x22 µm^2. One additionally explored channel had a cross section of 55x22 µm^2. Observations were made at X=1 cm, with the channel placed on an inverted microscope (Nikon), with a 100x /oil objective offering a (X,Y) field of view of 87x 66 µm^2. An UltraView Confocal Laser Scanning system (Perkin Elmer) was used to visualize the fluorescent particles. The focal Z-plane was chosen halfway between floor and ceiling to ensure the absence of velocity gradients in the vertical direction. The number of localized particles per image was approximately 130 for ϕ= 0.03 and 1500 for ϕ= 0.3, respectively.

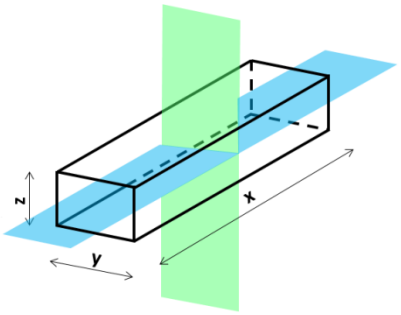

Figure 1: Schematic of the 3D channel geometry and coordinate system with X (horizontal, flow), Y (horizontal, perpendicular to flow) and Z (vertical). Respective dimensions of the channel: 2 cm, 30 µm and 22 µm. Video recordings were taken in (X,Y) planes at Z=11 µm (for reasons of symmetry).

Typical movie stills for the suspension at low and high volume fractions are shown in Fig. 2. Due to the refractive index matching, particles are well resolved, even at Z=11 µm and ϕ= 0.3. Particle localization was performed with the publicly available software written in IDL language [39]. The spatial resolution was approximately 0.1 pixel length, for effective pixels of 135x135 nm^2. Smearing of the intensity profiles (as in [40]) turned out to be modest even at the highest explored flow rate. Movies consisted of 500 frames for ϕ= 0.3, and 1500 for ϕ= 0.03. Images were acquired at 15 fps (Δt=0.067 s). During data analysis we discovered that incidentally (once per 10-20 frames) images had not been stored. These errors were identified via the occurrence of instantaneous flow velocities that were twice as high as most others, and repaired by reassignment of the time array, followed by interpolation of the affected trajectories. In subsequent calculations of MSDs these interpolated data were taken out again.

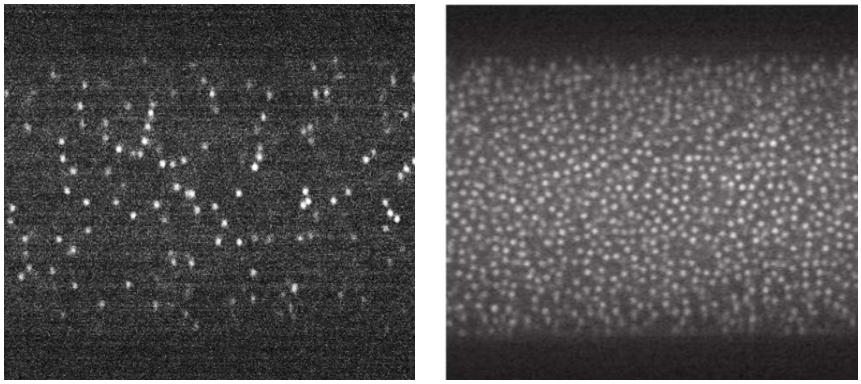

Figure 2: Typical images of particles flowing through channels at φ= 0.03 (left) and φ= 0.3 (right).The channel width is 30 μm.

3. SIMULATIONS

To mimic experimental data, particles were generated and displaced inside a box of 600, 200 and 10 pixels along X, Y and Z respectively. Each particle was modeled as an object of 8x8 (x,y) pixels to allow excluded area interactions, and a mass center at a certain (x,y,z) location to enable tracking. The total area fraction (AF) in the (x,y) plane was set via the number of particle centers N_{pc} in the (x,y) range of the box: AF $\approx$ (64/1.2 10^5)*N_{pc}. Before each time step, particles had to be added: initially to fill the box with N_{pc} particles, and in the next steps to make up for particles that had left the box. Particles were introduced one-by-one using uniform random generators for the (x,y,z) coordinates, and were rejected if (x,y) area overlap (at pixel level) occurred with existing ones. In each time step, particles were displaced via diffusive steps in the X, Y and Z directions using a Gaussian random generator with imposed standard deviations σ_x, σ_y and σ_z, plus a advective step in the x-direction using the imposed parabolic velocity profile $v_x(y)$. Disappearance of particles (centers) occurred via (x) flow and/or (x,y,z) diffusion.

A systematic variation was made of the diffusion coefficient and the maximum advective velocity, varying $\sigma_x=\sigma_y=\sigma_z$ from 0.2 to 1.0 pixel, and choosing v_{max} between 0 and 8.0 pixel/frame. This upper limit is already beyond practical values for 8 pixel sized particles (it would give a severely smeared image). Explored area fractions were 0.032, 0.32 and 0.43. To enable direct comparisons, the product of N_{pc} and the number of time steps was kept constant at 10^6. Data were generated in the matrix format as required by the standard tracking software [39], replacing of one of the unused columns to give each particle a unique identifier.

4. DATA ANALYSIS

In our analysis, particle trajectories are obtained in a coordinate system attached to the laboratory. Relative to this system the microscope table exhibits a (slow) motion. The aim of the measurement is to find the motions of the particles relative to the table. Some of the concepts that we used, like the division into flow-lanes and subtraction of estimated advection prior to tracking, show similarity to those described in an excellent review paper [33]. However the here presented 'iterative masking' method that uses particle coordinates only (Sec. 4.1.1-3) is new. Furthermore our approach involves specific choices and details which need to be specified in order to fully appreciate the analysis. Operations will be described both verbally and mathematically to facilitate implementation.

4.1 Tracking particle displacements

The procedure starts with localizing all particles in each video frame, as usual in particle tracking microrheology [41, 42]. Taking the list of coordinates and times as input, iterative tracking is used to find the time-averaged velocity profile and the particle trajectories. Thereafter it is possible to correct separately for transients in flow rate and for table drift perpendicular to the flow. Subtraction of the instantaneous advective displacements from the 'real' trajectories produces so-called 'residual' trajectories, from which MSDs in the X and Y directions are calculated. This procedure is illustrated in Fig. 3 and explained in more detail below.

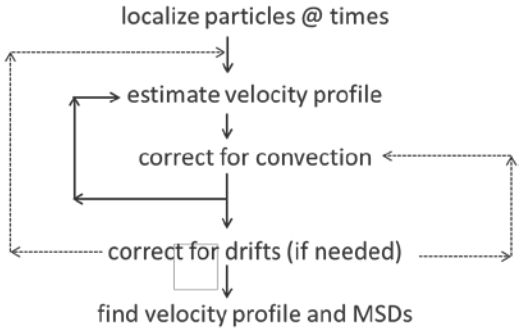

Figure 3: Schematic of the procedure to find the particle trajectories. Dotted arrows indicate optional corrections for different types of drift (see text).

4.1.1. Identifying particle displacements

To identify the particle displacements, the standard method for materials in the quiescent state [35] is modified. An iterative procedure is used, in which tracking is initially restricted to Regions Of Interest which are aligned along X (see Fig. 4). These ROIs will be called Y-bins since they are specific for a certain Y (range). The length of each Y-bin is given by the X-range $(x_{max}-x_{min})$ in which particles are detected, while its width ΔY is defined by the total Y-range and the chosen number of bins N_y:

$$\Delta Y = (y_{max} - y_{\min})/(N_y - 1) \quad (1)$$

Particles that remain in the same Y-bin during a time step are then identified by standard tracking [39] within a search radius Δr_{max} corresponding to the maximum allowed displacement:

$$(\Delta x)^2 + (\Delta y)^2 \leq (\Delta r_{\max})^2 \quad (2)$$

where Δx and Δy are the distances between a particle at time t_k and a particle (in the same Y-bin) at time t_{k+1}. When dealing with high number densities and large x-displacements, an appropriate combination of ΔY and Δr_{max} has to be chosen for the tracking to be successful. Else the search-area around a given particle at time t_k will be contaminated by other particles at time t_{k+1} due to the advective transport. To avoid the ensuing correlation problem (leading to crashes of the algorithm) the Y-bins have to be chosen narrow, but still wide enough to allow measuring a few displacements. This works because the most probable diffusive displacements in the y-direction are the smallest ones (illustrated in Fig. 13).

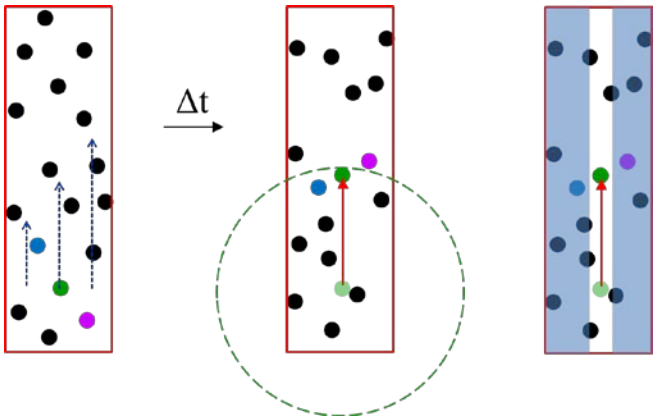

Figure 4: Cartoon of the first step of the tracking procedure. The box is aligned with the flow direction (X). In the left panel, arrows indicate the local flow velocities. The middle panel shows how the particle configuration changes over a unit time step Δt (mainly due to advection). To find the displacement of the green particle, the tracking algorithm needs a minimum search radius as indicated. Other candidate-particles are filtered out by the judicious masking as shown in the right panel. The non-masked flow-lane is called a Y-bin.

To allow a widening of the bins, and hence a more complete detection of the displacements in the next iteration, use is made of the best available knowledge about the velocity profile. Initial estimates for $v_x(y)$ are used to modify the x-coordinates of the particles at time t_{k+1} before comparing them to the coordinates at time t_k:

$$x_i'(t_{k+1}) = x_i(t_{k+1}) - v_x(y_i(t_k))\Delta t \qquad (3)$$

where i labels a particle, Δt is the unit time-step and $v_x(y)$ is interpolated at $y=y_i$. This operation, which 'biases' the search towards finding the correct displacements and also allows use of a smaller Δr_{max}, is illustrated in Fig. 5. After finding which coordinates (x,y) at time t_k and (x',y') at time t_{k+1} belong to the same particle, the advection correction of the x-coordinates at time t_{k+1} is undone to enable a similar comparison between times t_{k+1} and t_{k+2}. We remark that this 'pairwise tracking' is the most rigorous way to remove the affine motion; algorithms that assume an average local velocity over multiple time steps could introduce errors, especially if trajectories are long and/or velocity gradients are large [43]. The obtained first estimate of $v_x(y)$ (see Sec. 4.1.2) is then used in the next iteration, and so on.

4.1.2. Finding the velocity profile

The advective velocity profile is estimated after dividing the y-range into bins as defined in Sec. 4.1.1:

$$y_s = y_{min} + i_s \Delta Y \quad \text{with} \quad i_s = 0 \ldots N_y - 2 \qquad (4)$$

With y_s the lower boundary of a Y-bin, and $y_s + \Delta Y$ the corresponding upper boundary. Standard tracking [39] is used to identify the displacements of those particles that remain in the same bin during a unit time step. Averaging over all particles and time steps then produces the mean local velocity in the x-direction:

$$v_x(y) = \sum_{i,k\in\{Y_s\}} \Delta x_i(t_k) \,/\, \sum_{i,k\in\{Y_s\}} \Delta t \quad \text{where} \quad i,k \in \{Y_s\} \quad \text{if } y_s < \{y_i(t_k), y_i(t_{k+1})\} < y_s+\Delta Y \qquad (5)$$

Here $\Delta x_i(t_k)$ is the displacement of particle i between t_k and t_{k+1}. To make the measurement of $v_x(y)$ slightly more accurate, the y-value assigned to $v_x(y)$ is set equal to the average y-position of the tracked particles (rather than the midpoint y-value of the bin).

Depending on the experiment and the iteration stage, the measured velocity profile may look noisy, due to the finite number of observations. In the first iteration, the Y-bins are usually chosen narrow. A relatively large fraction of the particles may then remain undetected because lateral diffusive steps take them into another Y-bin. Other reasons for poor statistics are a low particle concentration or a short duration of the experiment. Noise is removed by a judicious smoothening. Velocity profiles are very often gradual, as required by the spatial continuity of the mechanical stress in the fluid.

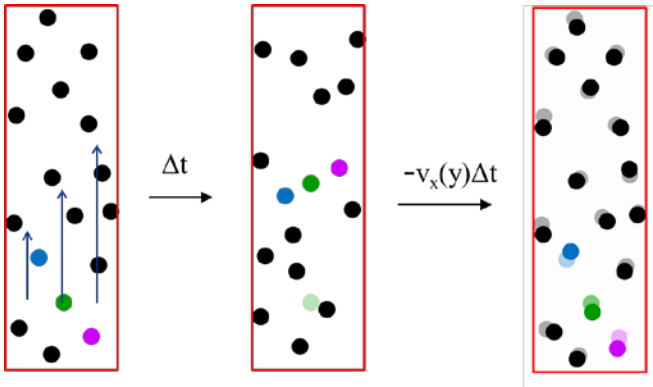

Figure 5: Cartoon of the second step of the tracking procedure. Particle configurations are compared before and after a unit time step Δt. The left and middle panels are similar to Fig. 4. The right panel shows that after correction for local advection, the residual displacements are much smaller. This allows use of a smaller search radius in the tracking step (compare the faded and non-faded dots). In this example the estimated $v_x(y)$ is already quite accurate.

4.1.3. Ending the iterations

Repeating operations as described in Secs. 4.1.1 and 4.1.2, results in progressively better estimates of the velocity profile and hence in more reliable tracking. The reason is that subtraction of the advective displacements before tracking, diminishes the probability of misidentifications. This was illustrated in Fig. 5 (right panel): locations of the same particle in subsequent frames will be closer, making it less likely that another particle happens to be even closer. The improved correction for affine motion also allows choosing a smaller Δr_{max} per iteration step. Ultimately, the smallest value for Δr_{max} will be dictated by the need to capture all the diffusive displacements. As long as the latter are smaller than the typical interparticle distance in the fluid, tracking should be possible [33]. Since the chance of finding a 'ghost particle' within the search radius strongly diminishes, also the need for restricting the tracking to Y-bins vanishes. Therefore in a typical iteration path, Δr_{max} is gradually reduced, while the bin with ΔY is increased. The (evolutions of the) values of these parameters are manually set.

4.1.4. Constructing trajectories

Trajectories are obtained by linking together all steps that were taken by the same particle:

$$x_i(t_j) = x_i(t_{i0}) + \sum_{k=i0}^{j} \Delta x_i(t_k) \quad \text{with} \quad \Delta x_i(t_k) = x_i(t_{k+1}) - x_i(t_k) \tag{6}$$

and likewise for displacements in the y-direction. In this (standard) expression, t_{i0} is the real time at the beginning of the particular trajectory. Specific for our method is that, because of the pairwise tracking (Sec. 4.1.1), the starting point of the linking operation is a set of single-step trajectories that contain (inherent) redundancies. Many particle-time records (x_i, y_i, t_k) occur twice: as the end point of

the step from t_{k-1} to t_k and as the starting point of the step from t_k to t_{k+1}. The trajectory labels l_t are different however. This problem is tackled by assigning an additional label l_k to each data record, so it will contain $(x_i, y_i, t_k, l_k, l_t)$. Multi-step trajectories are then created by a clustering operation that first groups all records that have either l_k or l_t in common, and subsequently eliminates the redundancies and assigns a new trajectory label. Optionally, this clustering operation can be aborted at a set maximum trajectory length; remaining locations of the involved particle are then analyzed as if they belong to a new particle. This option can be useful in the calculation of y-dependent MSDs (Secs. 4.3 and 5.3.2).

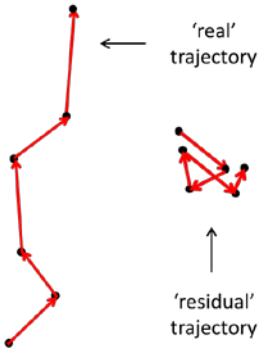

Figure 6: 'Real' and 'residual' trajectories. The latter are obtained from the former by subtraction of the instantaneous advective motion.

4.2. Removing advection

For statistical analysis of the stochastic displacements, the advection needs to be removed from the trajectories. This is achieved by subtracting from each $\Delta x_i(t_k)$, the measured average displacement in the x-direction, at the instantaneous *y*-location $y_i(t_k)$:

$$x_i'(t_j) = x_i(t_j) - \sum_{k=i0}^{j} v_x(y_i(t_k))\Delta t \qquad (7)$$

where $v_x(y_i)$ is interpolated from the measured velocity profile (as before). This operation keeps the trajectories intact, but the displacement steps $\Delta x'_i(t_k) = \Delta x_i(t_k) - v(y_i(t_k))\Delta t$ should now become purely stochastic. Note that displacements in the *y*-direction remain unaffected. The difference between the 'real' trajectories $r_i(t_k \ldots t_j)$ and the 'residual' trajectories $r'_i(t_k \ldots t_j)$ obtained using Eq. 7 is illustrated in Fig. 6.

In case of a time-dependent flow, the following extension is made:

$$v_x(y,t) = v_x(y) * f(t) \qquad (8)$$

where

$$f(t_k) = \sum_{iy=1}^{N_y} \frac{v_x(y(iy),t)}{v_x(y(iy))} / N_y \quad \text{with} \quad y(iy) = y_{min} + (iy-1)\Delta Y \qquad (9)$$

Here the ΔY corresponds to a new binning of the Y-range (optimized for measuring fluctuations in flow rate). The idea behind this binning is to reduce the sensitivity of $f(t)$ to dis/appearances of particles in/from flow lanes with low or high speeds. In words, Eq. 8 means that the flow rate is considered time-dependent, but the shape of the velocity profile assumed to remain the same.

4.3. Calculating Mean Squared Displacements

Given the advection-free trajectories, calculation of the Mean Squared Displacements in the x- and y-directions is straightforward. In channel flow the MSDs may depend on the y-location, due to possible influences of walls and velocity gradients [36]. Measurement of this dependence is done by calculating for each trajectory *i* the average y-location $\langle y \rangle_I$, and using the distribution of the found $\langle y \rangle$ values as a basis for making a new binning of the Y-range (now optimized for measuring MSDs). In equation form:

$$\langle y \rangle_i = \sum_{ki0}^{k_{imax}} y_i(t_k) / \sum_{ki0}^{k_{imax}} \quad (10)$$

where k_I labels the real time (or frame number): k_{i0} is the beginning of the particular trajectory while $k_{imax+1} - k_{i0} + 1$ is its length. The local x-MSD in a particular Y-bin is then given by:

$$MSD_{x'}(y, n\Delta t) = \sum_{i_{\langle y \rangle \in \{Y_s\}}} \sum_{k=i0}^{k_{imax}-n} [x_i'(t_{k+n}) - x_i'(t_k)]^2 / \sum_{i_{\langle y \rangle \in \{Y_s\}}} \sum_{k=i0}^{k_{imax}-n} \quad (11)$$

where $n\Delta t$ is lagtime, and the y-locations have to fall between the boundaries of the bin:

$$i_{\langle y \rangle} \in \{Y_s\} \quad \text{if } y_s < \langle y \rangle_i < y_s + \Delta Y \quad (12)$$

The y-position of the bins itself is taken at the midpoint between the boundaries. In the calculation of the *y*-MSD, x'_i has to be replaced by y'_I in Eq. 11.

While the calculation of the MSDs according to Eqs. 10-12 is fairly simple, and can be achieved with the standard routine [39], there are two specific points of attention. Firstly, the Y-binning (or Y-resolution of the MSD) has to be chosen judiciously: this is a matter of the number of displacements steps and possibly also the distribution of the latter over the entire y-range. Secondly, for long trajectories, $\langle y \rangle_i$ may no longer be completely representative for the Y-bin as assigned via Eq. 12: the particle might have visited neighboring Y-bins as well. Compromises in the y-resolution of the MSD arising from this effect can be mitigated by segmentation of trajectories into fragments with a preset maximum length (Sec. 4.1.4).

5. RESULTS AND DISCUSSION

5.1. Computer simulations

Since the computer simulations provided possibilities to test our analysis method for a broader range of parameters, we discuss most of our results here. Roughly speaking, two performance levels can be identified; the first level being a correct measurement of the velocity profile via particle tracking, and the second (more demanding) level comprising the measurement of the reliable MSDs via careful subtraction of the local advection.

All simulated datasets were analyzed with the same parameter settings. Four iterations were used to obtain the trajectories, reducing the number of Y-bins (flow lanes) sequentially as 100, 40, 10, 3 and the corresponding maximum displacements (search radii) as 8, 4, 4 and 4 pixels. Typically only results of the last iteration will be presented. Areas close to the boundaries of the final 3 Y-bins used during tracking, were excluded from the analysis, to avoid negative biasing of the found D_y values. In the construction of trajectories, the length was maximized to 12 steps; longer trajectories were cut into units of 12 steps, which were then treated as individual trajectories. This was supposed to contribute to a more even spreading of the mass-centers of the trajectories over the available y-range, and also

to a better y-resolution of these quantities (Sec. 4.3). Mean Squared Displacements were fitted with a linear function using the first 7 lag times, after which the slope was taken as the measured diffusion coefficient, following the Einstein relation.

5.1.1. Velocity profiles

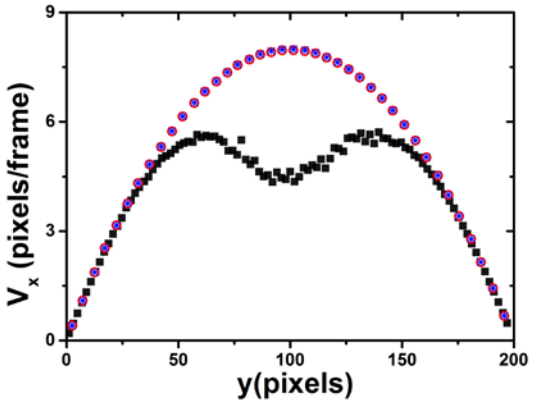

Figure 7: velocity profile for v_{max}=8.0 pixel/frame and D_x = 0.36 pixel^2/frame at AF=0.32, measured in 3 iterations: 1) black squares, 2) red circles, 3) blue stars.

Measurement of the velocity profiles turned out to work successfully for all explored conditions, without the need for (nonzero) initial estimates for $v_x(y)$. An issue at low concentration (AF=0.032) was the occasional occurrence of empty Y-bins (for the entire time range) in the first iteration. This was addressed by deleting the data points for these bins; the ensuing problem of gapped $v_x(y)$ data in the next iteration was automatically handled by the software via interpolation between the available data points. Convergence of the velocity profile was always reached within 3 iterations; in most cases the first 2 measurements already superimposed well. Exceptions were only found in cases where v_{max} exceeded 6 pixel/frame. Fig. 7 shows the stepwise improvement for a simulation at the highest flow rate. Although the first used Δr_{max} equals the largest advective displacement (8 pixels), the initially measured velocities are lower. This can be due to two effects: i) additional diffusive displacements cause Δr *to* exceed 8 pixels, or ii) another particle in the same Y-bin is trailing so closely that its displacement brings it closer to the original position of the leading particle than the leader itself. In the latter case, which most likely occurs at the highest velocity, the ensuing misidentification leads to a measured displacement in the negative flow direction; this explains the dimple in the initial $v_x(y)$. In subsequent iteration steps this error is rectified by biasing the search towards forward displacements. Additionally, the measurement accuracy also is improved stepwise via the larger total number of particles that are tracked as the Y-bins are made wider. For low particle concentrations, the finally obtained $v_x(y)$ is relatively less accurate, even though the number of data records was the same (10^6); this can be seen by comparing Fig. 7 and Fig. 9.

5.1.2. Diffusion coefficients

The diffusion coefficients extracted from the simulated data were inspected using graphs of D_x ($=\sigma_x^2$) and D_y ($=\sigma_y^2$) as a function of y. Exploring broad ranges of diffusion coefficients (0.04-1.0 pixel^2/frame) and flow velocities (0-8 pixel/frame) at 3 discrete area fractions (0.032, 0.32, 0.43), we found that the inputted (equal and y-independent) D_x and D_y were fairly well recovered in the majority of cases.

General trends

Typical results are illustrated in Figure 8 for AF=0.32, v_{max}=8 pixel/frame, and a variety of diffusion coefficients. In all cases statistical noise is encountered, as illustrated by the 'spiky' nature of the variation with y, and the lack of a perfect symmetry with respect to y=0. Variation of the number of data records confirmed that the noise can be progressively reduced by increasing this number. A constant value of 10^6 was chosen for all simulations presented here. Besides this random noise, also systematic dependences of the relative errors in D_x and D_y on the magnitude of the diffusion coefficient and on the y-location appear present.

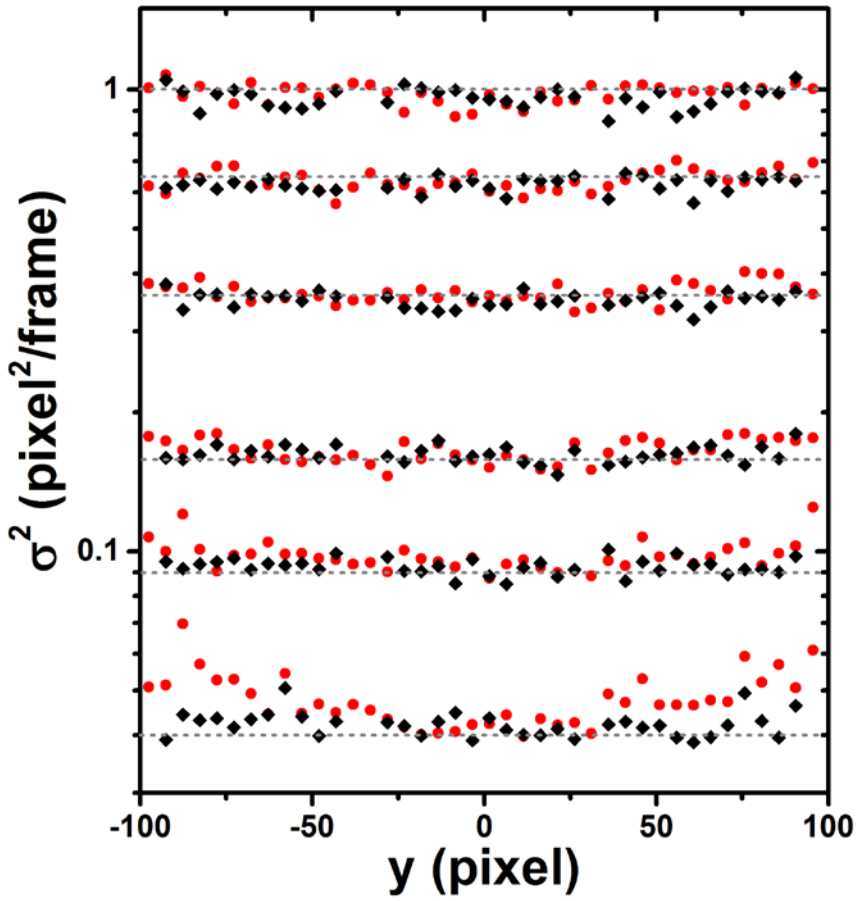

Figure 8: Measured diffusion coefficients σ^2_x (red circles) and σ^2_y (black diamonds) compared to input values (dashed lines) in a simulation where particles are advected via a parabolic profile (symmetric around Y=0) with a maximum velocity of 8.0 pixel/frame, and additionally show diffusion with coefficients ($\sigma_x=\sigma_y=\sigma_z$) of 0.04, 0.09, 0.16, 0.36, 0.64 and 1.0 pixel. Area fraction is 0.32.

One systematic error observed for the largest diffusion coefficients, is that the measured D_x and D_y fall slightly below their input values. This effect, which is noticeable for D=0.64 and 1.0 pixel^2/frame in Fig. 8, is due to the use of Δr_{max}=4 pixels in the last iteration. Even though this number is significantly above the standard deviation σ of the Gaussian diffusive displacements (0.8 and 1.0 pixels), the rejection of displacements Δr>2.83σ (respectively 3.16σ) still lowers the measured second moment (i.e. the MSD of a single step) by as much as 15% (7%). Mitigation of this issue by choosing a larger Δr_{max} would be possible for the lower area fraction of 0.032, but at high area fractions the correlation problem described in Section 4.1.1 then shows up.

A second systematic error is found for D_x, which shows a positive deviation at combinations of small D_x , large $|y|$ and high flow rates. This is observable in Fig. 8 (corresponding to the highest flow rate) for σ_x^2=0.04 and 0.09 pixel^2/frame. Considering that in our case the shear rate is proportional to $|y|$, a plausible explanation might be the occurrence of small diffusive displacements Δ_y in the y-direction. An undetected diffusive step into a different flow lane would cause an error in the subtracted advection and hence an overestimation of the x-MSD. A velocity error $\Delta_y \dot{\gamma}$, then changes the x-MSD:

$$<(\Delta x)^2>(\tau) = (\sigma_x^2 + (\sigma_y \dot{\gamma})^2 \tau_0)*\tau \ , \qquad (13)$$

where τ_0=1 frame since the v_x-value used in the advection correction was evaluated for each individual time step (see Eq. 7). For σ_x=σ_y and $\dot{\gamma}$=0.16/frame (the highest shear rate), Eq. 13 predicts a 3% increase in apparent D_x, which is much lower than the one observed in Fig. 8. Moreover Eq. 13 also indicates that the relative error should be the same for all σ, which is not in line with the trend observed in Fig. 8. Alternatively, an inaccuracy Δv_x in the measured local velocity $v_x(y)$ would produce an x-MSD given by:

$$<(\Delta x)^2>(\tau) = (\sigma_x^2 + (\Delta v_x)^2 \tau)*\tau \qquad (14)$$

For relatively small Δv_x and τ, the quadratic term will not be prominent, but it can still contribute significantly to the apparent D_x as found by fitting the x-MSD with a linear dependence on the lag time. Clearly the error should become most noticeable at small σ_x. Taking the (worst) case of σ_x^2=0.04 pixel^2/frame and Δv_x=0.06 pixel/frame (a typical number from the simulation data), a 70% increase in apparent D_x is obtained from a linear fit to Eq. 14. This noise level is in reasonable agreement with Fig. 8. Also for the lower flowrates a fairly good agreement with Eq. 14 is found (not shown).
The remaining question, why the error increases with $|y|$ can be addressed by considering that near the walls, the flow velocities are lower. Particles flowing there have a longer residence time in the simulation box, and hence are not refreshed as often. Especially in combination with a low σ_y and σ_z (which tend to keep particles in the same y-bin and focal z-plane) this leads to a relatively poor sampling of the y-range and hence a less accurate measurement of the local $v_x(y)$. Recalculation of the x-MSDs, now using the (perfectly parabolic) input velocity profiles to eliminate the convection, produced a strong reduction of the y-dependent error in D_x. This finding, illustrated in Fig. 9, corroborates that indeed the direct error in Δv_x is responsible.

Specific issues at low and high concentrations

While it is clear from the above that the measurement of accurate (x-) MSDs is generally more difficult at high flow velocities and low diffusion coefficients, it also appears that the regimes of low and high particle concentrations present their own specific issues.

At small area fractions, noise in the velocity profile (Eq. 14) is a prominent source of error. Even when taking the number of time steps inversely proportional to the number of particles per frame (to keep the product constant at 10^6), the obtained $v_x(y)$ data are more noisy at low AF. Here the y-bins become less evenly populated, giving less accurate measurements of v_x in the most underpopulated bins. The origin lies in the random insertion of new particles. At higher AF, these are less random because the area exclusion between particles leads to many rejections, thus favoring the more empty areas for insertions of new particles. The effect of a noisy $v_x(y)$ on the measured D_x is illustrated in Fig. 9.

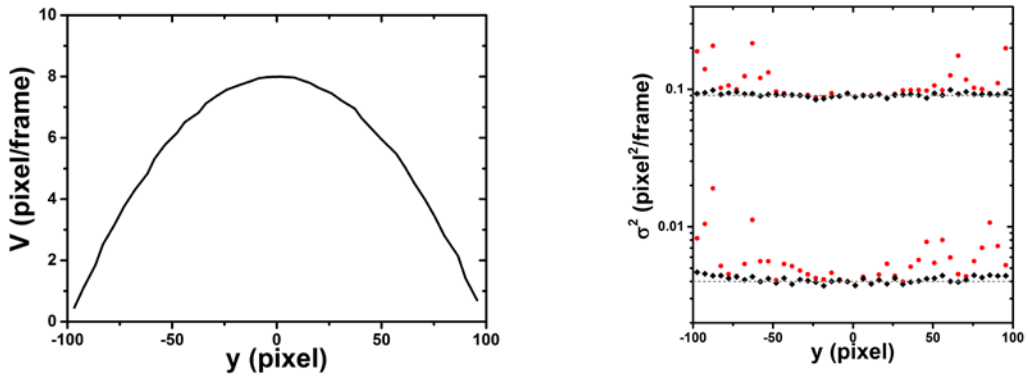

Figure 9: Effect of errors in the measured flow velocity on the measurement of σ_x^2 at low concentration (AF: 0.032). Left: measured velocity profile for v_{max}=8.0 pixel/frame and σ_x^2= 0.04 pixel^2/frame. Right: apparent $D_x(y)$ based the measured (red dots) and the ideal (black diamonds) $v_x(y)$, for σ_x^2=0.04 and 0.09. The former data have been multiplied with 0.1 to improve the clarity of the plot.

At large area fractions (AF=0.43), the main source of error is misidentification, i.e. the occurrence of found trajectories that involve more than one particle. The fraction of thus flawed trajectories was determined by detecting for changes in particle identifier within a trajectory, and was found to increase non-linearly with particle concentration: for AF=0.032 it is always < 10 ppm, making its contribution to the errors in the MSD negligible. However for AF=0.32 it can increase up to 1.6% while for AF=0.43 it can reach up to 7.6%. This is illustrated in Table 1 and Fig. 10.

Table 1: Fraction of trajectories (expressed as %) that contain one or more link-up errors, as a function of v_{max} and σ, for area fractions of 0.32 (left) and 0.43 (right).

AF =0.32

	v_{max}	0	2	4	6	8
σ						
0.2		0.022	0.042	0.068	0.085	0.12
0.3		0.070	0.099	0.13	0.17	0.20
0.4		0.16	0.20	0.23	0.26	0.30
0.6		0.48	0.50	0.53	0.58	0.61
0.8		0.93	0.95	1.0	1.03	1.1
1.0		1.5	1.5	1.5	1.6	1.6

AF=0.43

	v_{max}	0	2	4	6	8
σ						
0.2		0.41	0.61	0.78	0.96	1.1
0.3		1.1	1.3	1.4	1.6	1.8
0.4		1.9	2.0	2.2	2.4	2.5
0.6		3.7	3.9	4.0	4.1	4.2
0.8		5.7	5.7	5.8	5.9	6.0
1.0		7.5	7.5	7.6	7.6	6.0

The explanation for this dependence on particle concentration is straightforward: in more crowded systems, particles occur in closer proximity, making it more likely that more than one particle will occur within the search-circle defined by Δr_{max}. Combined with the random (x,y) displacements of these neighboring particles, this leads to increased chance of misidentification. The clear dependence of the error fraction on σ in Table 1 is also consistent with this picture: a larger diffusion coefficient will lead to more 'scrambling' (just as in a quiescent system). The dependence of the error on v_{max} is relatively weak, and shows a clear trend only for low diffusivities: if the random displacements are small, then cases leading to particle misidentification will mainly be generated via differences in advection; the probability of this effect increases with the shear rate and hence with the maximum velocity.

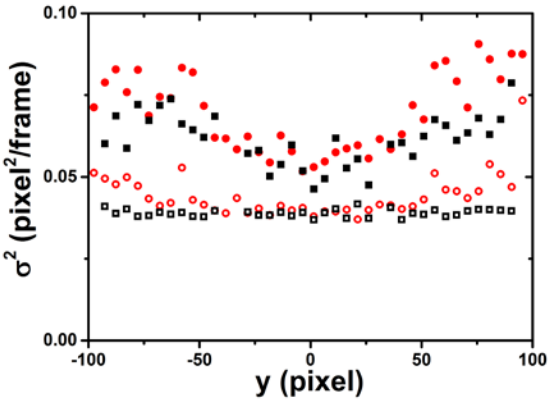

Figure 10: Effect of tracking errors on measured diffusion coefficients at high concentration (AF =0.43). Maximum flow velocity is 8.0 pixel/frame, diffusion coefficient is 0.04 pixel²/frame. Red dots correspond to D_x, black squares to D_y. Closed symbols show the results of the analysis, while the open ones were calculated after removing the flawed trajectories.

Finally we present overall accuracies in the measured diffusion coefficients for all 90 flow experiments that were simulated. Since we did not aim for a spatially resolved overall analysis and because a 'break down' of the errors into specific mechanisms (as done above) is not always possible, we present results that are lumped over the entire y-range. Specifically, for the data sets shown in Fig. 8 and similar for all other flow rates, the difference between the locally measured D and the level of the dashed line was taken as the local error. From the local errors within the same data set, Root Mean Squares were calculated, and presented in Table 2.

The trends in this Table mostly confirm the expectations: relative errors are largest for small diffusivities and high velocities. Comparing Tables 1 and 2, it becomes clear that tracking errors are most influential for low diffusivities, even though the fraction of misidentified trajectories is larger for high diffusivities. This is attributed to the relative importance of the misidentified displacement: assuming that it will have a typical magnitude comparable to the interparticle distance, the anomaly of such a displacement will be stronger if the typical diffusive displacements are smaller. This issue, and its possible mitigations, have been described in [44].

While the precise numbers in the Tables will clearly vary with the chosen y-binning of D_x and D_y, and could show (weak) dependence on particular details of the simulations as well (e.g. the z-range of the simulation box), the trends of the errors are believed to be correct, and the typical magnitudes in the right range. As such they could be useful as a guideline in designing experiments. Since σ and v_{max} are expressed in pixels and frames, translation of these results to an optimized pixel binning and exposure time for a specific experimental situation should be relatively straightforward.

Table 2: Aggregated relative errors in diffusion coefficient along x (top) and y (bottom). AF is the area fraction occupied by the particles, σ is the standard deviation of the diffusive displacement and v is the flow velocity at the centerline of the channel.

AF=0.032

Dy	v	0	2	4	6	8
σ						
0.2		2.8	3.3	3.7	3.3	3.2
0.3		2.7	3.2	3.9	3.9	4.4
0.4		3.2	3.6	4.2	3.4	3.5
0.6		3.5	3.4	3.9	3.3	3.0
0.8		4.2	3.8	4.7	3.8	3.5
1.0		4.5	5.1	5.3	4.4	4.6

AF=0.32

Dy	v	0	2	4	6	8
σ						
0.2		3.8	4.2	5.5	6.2	8.7
0.3		2.8	4.5	4.4	4.6	5.1
0.4		3.9	3.3	3.3	2.8	4.4
0.6		4.6	5.2	4.2	5.2	4.5
0.8		5.0	6.3	4.4	5.5	4.3
1.0		5.9	6.0	7.4	6.8	6.1

AF=0.43

Dy	v	0	2	4	6	8
σ						
0.2		18	30	42	48	57
0.3		16	18	22	28	32
0.4		11	11	16	16	19
0.6		5.4	4.7	6.8	7.3	7.0
0.8		4.9	5.0	5.9	4.6	5.3
1.0		8.1	8.0	7.8	8.0	6.6

AF=0.032

Dx	v	0	2	4	6	8
σ						
0.2		3.1	5.9	22	27	85
0.3		4.2	8.1	12	16	46
0.4		2.9	3.2	5.8	9.8	20
0.6		3.2	3.5	3.0	4.1	7.8
0.8		3.9	3.3	3.2	3.3	3.9
1.0		3.4	4.3	3.4	2.7	4.6

AF=0.32

Dx	v	0	2	4	6	8
σ						
0.2		4.1	5.2	9.6	18	25
0.3		3.8	3.0	5.7	8.3	12
0.4		3.6	2.9	3.8	4.7	6.9
0.6		4.9	4.4	4.7	4.2	4.9
0.8		6.5	5.3	4.8	5.6	4.9
1.0		6.1	6.1	5.8	4.8	5.0

AF=0.43

Dx	v	0	2	4	6	8
σ						
0.2		19	34	45	72	80
0.3		14	20	29	34	42
0.4		9.6	13	19	21	27
0.6		4.6	5.6	7.3	8.5	12
0.8		4.2	4.5	4.6	6.1	6.2
1.0		6.4	6.4	5.9	5.2	5.2

5.3. Experiments

To further validate our analysis, we also applied it to experiments in a microfluidic channel. In this case also other potential sources of error can play a role, e.g. the quality of the imaging, the precision of the localization, drift of the microscope table and fluctuations in the flow rate. We demonstrate for a typical case that most of these errors can be kept small, or corrected for.

5.3.1 Velocity profiles

Measurement of the velocity profile was achieved within 3 iterations for all experiments. The highest velocity (at the centerline of the channel) amounted ≈8 μm/s, corresponding to ≈4 pixels/frame. The same parameters were used throughout the analysis, varying the number of Y-bins sequentially as [100,50,25] and the corresponding search radius (in pixels) as [6,4,3]. Here 100 Y-bins corresponded to a bin width of 0.3 μm, equivalent to 0.3 particle diameters or 2.2 pixels. In all cases, the first estimate of $v_x(y)$ was already close to the final one: see Fig. 11 for an example.

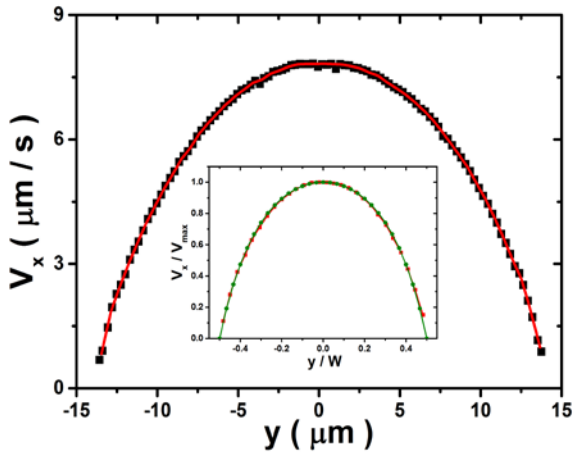

Figure 11: First (black symbols) and second iteration (red line) of a velocity profile measured at low volume fraction. First measured velocities are slightly underestimated in the center of the channel. Inset: comparison of the second measured $v_x(y)$ with a calculation for a Newtonian fluid (dots).

As shown by the inset if Fig. 11, the last iteration of the measured velocity profile corresponds well to a theoretical calculation [45] for a Newtonian fluid that is pumped through a rectangular channel of the same dimensions. Since dilute suspensions of hard spheres also show Newtonian behavior [46], the close correspondence further validates our method for measuring $v_x(y)$.

5.3.2 Mean Squared Displacements

Fig. 12 shows some representative Mean Squared Displacements (along the x- and y-directions) as obtained from the 'residual trajectories', after segmentation into fragments with a maximum length of 15 steps (see Sec. 4.1.4). All data sets correspond to the same experiment (the same fluid, pressure drop and z-coordinate), but different y-locations inside the channel (excluding points within 5 µm from the wall). A correction for minor (≈1%) variations in flow rate (see sec. 4.2) was performed before calculating the MSDs.

Several observations can be made. Firstly, the differences between the MSDs taken at different y-locations are generally rather small. Secondly, the majority of x- and y-MSDs turn out to be equal within statistical accuracy. Both findings indicate that the stochastic motion that remains after removal of the affine motion, is isotropic as for a quiescent fluid. Moreover, inspection of (the first 8 points of) each MSD reveals that they show good linearity, as expected for Brownian motion in a Newtonian liquid. This indicates that they can be considered as a measurement of the viscosity, for which we find ≈ 106 mPa.s using the Einstein relation.

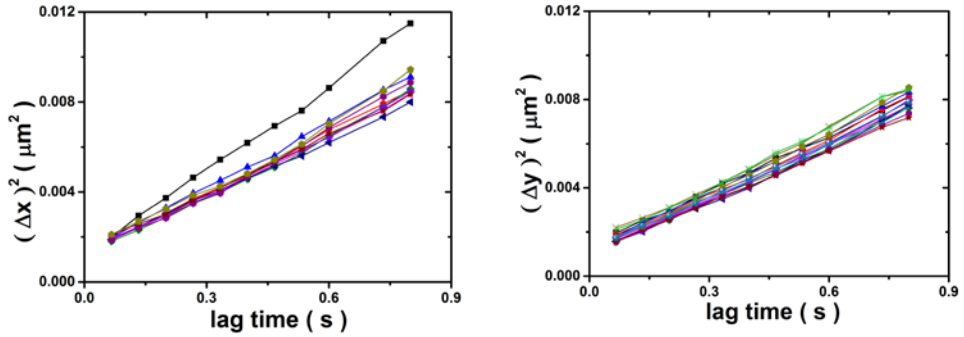

Figure 12: Mean Squared Displacements along X and Y directions for the experiment shown in Fig. 11.

The same residual trajectories were also analyzed for the probability displacement functions. The results obtained for the central flow lane (y=0) are presented in Fig. 13, show that the distributions are Gaussian for both the x- and y-directions. Also these data coincide well with each other. This corroborates once more that the elimination of the advective motion was successful.

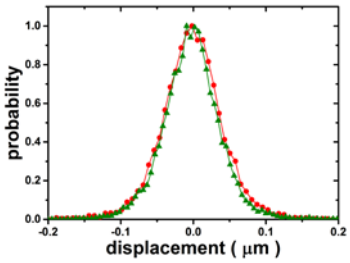

Figure 13: displacement probability functions for the x (red) and y (green) directions, measured at y=0 ±1 µm for the same experiment as shown in Fig. 11.

Returning to Fig. 12, we remark that extrapolation of the MSD data to zero lagtime always results in a (positive) non-zero ordinate. This deviation from the Einstein relation is attributed to limitations in the accuracy of the particle localization, as discussed in ref [41]. Note that the offsets are small: taking $2*10^{-3}$ µm^2 as a typical number, gives a square root of 44 nm, which seem reasonable as an error, considering the image quality that could be obtained (Fig. 2). In the calculations of diffusion coefficients from the MSD data (see below), this offset has been treated as a 'noise floor'.

5.3.3 Corrections for drift

Table drift

Correction for drifts can be important in experiments with a long duration. In our experiments, drift of the microscope table occurred with a typical velocity v_d of 0.01 pixel/frame, corresponding to ≈2 nm/s (per direction). By default, drift in the flow direction ends up in the measured $v_x(y)$. Separate measurement and correction could be done using a 'marker', like a particle that is stuck to a side wall of the channel [47, 48]. However for the present work, even the effect on the x-MSD was negligibly small. For the same reason, table drift in the Y-direction had a negligible influence on the y-MSD. In principle, y-drift can also affect the y-resolution of $v_x(y)$ through convolution with a function of width v_dT, with T the duration of the experiment. For the longest experiment (T=100 s) in this study this gives a width of ≈ 0.2 μm which is again negligible. For more narrow channels and/or longer lasting experiments the correction might still be needed. In that case, the average particle displacement in the y-direction has to be measured frame by frame, smoothened and integrated over time as in the usual drift correction [39]. The obtained function $\Delta y(t)$ should then be subtracted from the time-dependent y-coordinates, after which the tracking needs to be redone.

Transient flow

Also transient flows can play a role, even if they are not evidently visible from the video images. Similar to the effect discussed in the context of Eq. 14, they cause an error in the subtraction of advection, which in case of high flowrates can cause appreciable errors in the x-MSD. In our experiments with straight channels (i.e. no constrictions or expansions) the transients involved only the amplitude of $v_x(y)$ and not its shape; this was concluded after comparing the velocity profiles of different time segments, and was attributed to transients in the pressure drop. We found that after mechanical disturbances, whether intended (e.g. a change of reservoir height) or not, at least 1 minute was needed to obtain a stable flow rate again.

Variations in flowrate can be detected relatively simply using the standard procedure that measures drift from the trajectories [39]. However *correction* for the effect necessitated a modification of the procedure, the reason being that in spatially varying (e.g. Poiseuille-like) flows, the center-of-mass velocity of the particle ensemble becomes more sensitive to sampling issues. We observed that (dis)appearance (via advection or diffusion) of a particle from a low- or high-speed flow lane can add significant noise to the center-of-mass velocity, in particular for dilute suspensions. The correction described by Eqs. 8 and 9 mitigates this effect by measuring and normalizing the time-dependent v_x in different Y-bins (with judiciously chosen width). Y-regions within 5 particle diameters from the channel sidewalls were excluded, because of the large relative error after normalization with a low velocity.

An illustration of the success of this approach is given in Fig. 14, which shows an experiment where the flow rate was found to increase by more than 20% after a mechanical disturbance. In this particular case, a channel with a width of 60 μm and a structured wall (for Y=3-8 μm) was used. The iterative measurement of the (time averaged) velocity profile shown in Panel a indicates that $v_x(y)$ could still be measured as usual, in spite of the large amplitude variations $f(t)$ shown in Panel b. In Panels c and d, x-MSDs before and after the correction for varying flow rate are compared. In this (admittedly extreme) case, the drift correction reduces the MSD down to a factor 1/6.

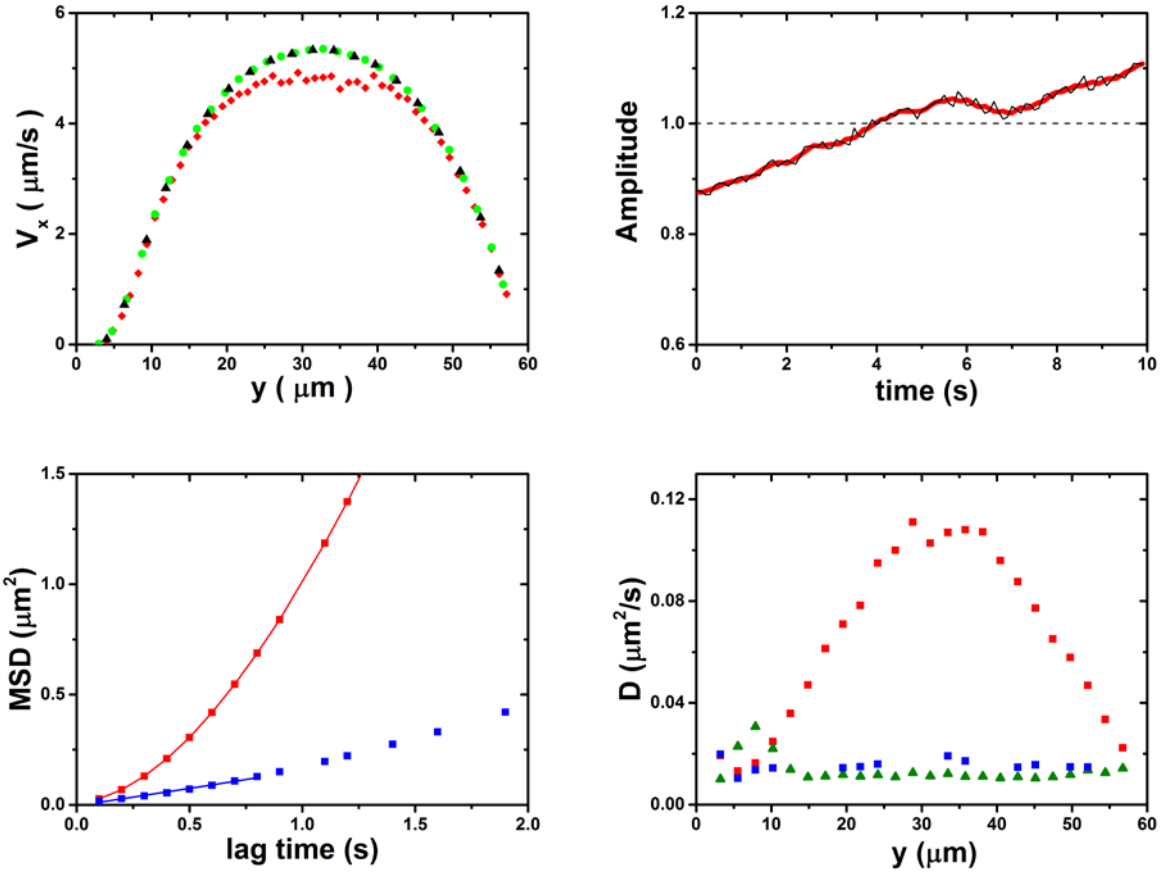

Figure 14: A case of time-dependent flow. Panel a: Velocity profile. Red diamonds, green dots and black triangles correspond to iteration 1, 2 and 3 respectively. Panel b: Time dependence of the normalized velocity. High-frequency noise (black line) is smoothened out (red line) before use of the signal to correct the trajectories. Panel c: MSD in the flow direction, before (red) and after (blue) the correction. These data were measured at Y=24 μm, where $\langle v_x \rangle$ = 5 μm/s (see panel a). Panel d: D_x before (red) and after (blue) correction, calculated from a linear fit to the first 8 points of the MSD. Green symbols indicate D_y. The volume fraction was 0.3 for this suspension.

5.3.4 Experiments at low volume fraction

A particular case that has hardly been considered so far, is the superposition of diffusion and shear flow of colloids in the dilute regime. Studies where colloids are used as flow tracers are well-known [19, 49] but also the diffusive motion contains information: under certain conditions mechanical properties of the local micro-environment can be inferred from the MSDs of the particles [24-26]. The case of colloids in a purely viscous environment provides first exploration of this potential application, by (effectively) measuring the viscosity η as a function of shear rate (since $D = kT/6\pi\eta a$). Data shown in Fig. 15 correspond to a dilute suspension (ϕ=0.03) of 1 μm silica spheres in water/ glycerol, flowing through a 30 μm wide microchannel with the velocity profile shown in Fig. 11. In comparison to the simulations, this experimental case contains additional (potential) contributions to the MSDs: localization errors and several types of drift, as well as hydrodynamic interactions between the particles. Inaccuracy in the localization, shown as the offset in Fig. 12, was taken into account by fitting the slope of the MSD. Variation in the flowrate (≈1% increase over the experiment) was mitigated using Eqs. 8 and 9.

First of all, the data show the expected overall trends: D_x and D_y appear to be equal to each other and independent of the local shear rate (exceptions indicated by triangular symbols are attributed to a wall effect [36]). This suggests that the advection and drifts were adequately subtracted, and that shear-induced hydrodynamic interactions, which would show a y-dependence [36] do not play any role of importance. Taking into account the outcomes of the simulations, the remaining noise level in D_x and D_y (or alternatively in η) is then most probably due to inaccuracies in the measured $v_x(y)$. Considering that in the experiment, $\sigma \approx 0.2$ pixel and $v_{max} \approx 4$ pixel/frame, we estimated the expected typical error level by doing calculations similar to those done for Table 2, but now adapted for the fewer datarecords and Y-bins. Thus we found expected relative errors of 5 ± 1 % for D_y and 35 ± 10% for D_x (where the $\pm$ sign takes into account the inaccuracy in σ) The noise levels in Fig. 15 are ≈15%, for both D_x and D_y, which is not in perfect agreement but of the correct order of magnitude.

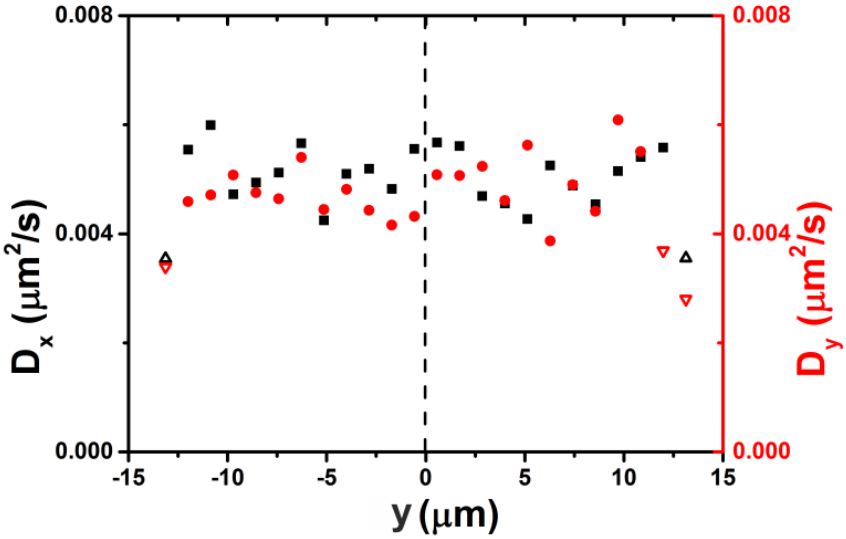

Figure 15: Diffusion coefficients in the x- and y-directions, measured as a function of the y-location in the channel, for the experiment shown in Figs. 11-13. D_x is plotted in black while D_y is plotted in red.

5.4. Comparison with other tracking methods

While the correction procedures and subsequent error analysis at the level of MSDs (Sections 4.2-5.4) have not been previously presented for colloids diffusing in a shear flow, the method to find the trajectories (Section 4.1) has elements in common with some of the procedures mentioned in ref [33]. A practical difference with the Correlated Image Tracking method is that our method only uses the images for particle localization, and subsequently tracks the particles using only their coordinates. In all cases addressed in this study, tracking was successfully achieved without the need for an initial estimate of the velocity profile: $v_x(y)=0$ provided a good enough start. CIT could be used in a slightly broader scope of applications, for example at are very high velocities: if the affine displacement within a flow lane becomes comparable to half the typical distance between particles, irreparable misidentifications would occur in the first iteration of our method. In that case, a crude (non-zero) estimate for $v_x(y)$ is needed, as could be generated with CIT. Both in ref [33] and in our work, CIT provides a suitable start, followed by an optional refinement at the level of the particle coordinates to achieve sub-pixel accuracy.

6. CONCLUSIONS

We developed an analysis, which extends and complements existing methods for tracking the advective and diffusive motions of colloidal particles in shear flow. Analysis of computer simulations and experiments indicates that our method can produce reliable results even for strong flows reaching local Peclet numbers of 50. Mean Squared Displacements, obtained by removing the instantaneous advective displacements from the trajectories, are sensitive both to the accuracy of the measured velocity profile and to the occurrence of tracking errors. As such, they provide on one hand a very suitable tool to validate the tracking, while on the other hand they indicate which level of accuracy is required to obtain reliable advection-free MSDs.

ACKNOWLEDGEMENTS

We thank Dirk van den Ende for discussions, and Daniel Wijnperlé for fabrication of the micro channels. This work was financially supported by NWO-CW (ECHO grant 09.FM.016).

REFERENCES

1. Shepherd, R.F., et al., *Microfluidic assembly of homogeneous and janus colloid-filled hydrogel granules.* Langmuir, 2006. **22**(21): p. 8618-8622.
2. Khan, S.A., et al., *Microfluidic synthesis of colloidal silica.* Langmuir, 2004. **20**(20): p. 8604-8611.
3. van Reenen, A., et al., *Integrated lab-on-chip biosensing systems based on magnetic particle actuation - a comprehensive review.* Lab on a Chip, 2014. **14**(12): p. 1966-1986.
4. Lowen, H., *Twenty years of confined colloids: from confinement-induced freezing to giant breathing.* Journal of Physics-Condensed Matter, 2009. **21**(47).
5. Semwogerere, D., J.F. Morris, and E.R. Weeks, *Development of particle migration in pressure-driven flow of a Brownian suspension.* Journal of Fluid Mechanics, 2007. **581**: p. 437-451.
6. Frank, M., et al., *Particle migration in pressure-driven flow of a Brownian suspension.* Journal of Fluid Mechanics, 2003. **493**: p. 363-378.
7. Sharma, M.M. and Y.C. Yortsos, *FINES MIGRATION IN POROUS-MEDIA.* Aiche Journal, 1987. **33**(10): p. 1654-1662.
8. Edmond, K.V., C.R. Nugent, and E.R. Weeks, *Influence of confinement on dynamical heterogeneities in dense colloidal samples.* Physical Review E, 2012. **85**(4).
9. Eral, H.B., et al., *Influence of confinement by smooth and rough walls on particle dynamics in dense hard-sphere suspensions.* Physical Review E, 2009. **80**(6).
10. Dettmer, S.L., et al., *Anisotropic diffusion of spherical particles in closely confining microchannels.* Physical Review E, 2014. **89**(6).
11. Nugent, C.R., et al., *Colloidal glass transition observed in confinement.* Physical Review Letters, 2007. **99**(2).
12. Fehr, T. and H. Lowen, *GLASS-TRANSITION IN CONFINED GEOMETRY.* Physical Review E, 1995. **52**(4): p. 4016-4025.
13. Conrad, J.C. and J.A. Lewis, *Structural Evolution of Colloidal Gels During Constricted Microchannel Flow.* Langmuir, 2010. **26**(9): p. 6102-6107.
14. Conrad, J.C. and J.A. Lewis, *Structure of colloidal gels during microchannel flow.* Langmuir, 2008. **24**(15): p. 7628-7634.
15. Isa, L., et al., *Velocity Oscillations in Microfluidic Flows of Concentrated Colloidal Suspensions.* Physical Review Letters, 2009. **102**(5): p. 4.
16. Isa, L., R. Besseling, and W.C.K. Poon, *Shear zones and wall slip in the capillary flow of concentrated colloidal suspensions.* Physical Review Letters, 2007. **98**(19).

17. Genovese, D. and J. Sprakel, *Crystallization and intermittent dynamics in constricted microfluidic flows of dense suspensions.* Soft Matter, 2011. **7**(8): p. 3889-3896.
18. Pipe, C.J. and G.H. McKinley, *Microfluidic rheometry.* Mechanics Research Communications, 2009. **36**(1): p. 110-120.
19. Degre, G., et al., *Rheology of complex fluids by particle image velocimetry in microchannels.* Applied Physics Letters, 2006. **89**(2).
20. Guillot, P., et al., *Viscosimeter on a microfluidic chip.* Langmuir, 2006. **22**(14): p. 6438-6445.
21. Moschakis, T., *Microrheology and particle tracking in food gels and emulsions.* Current Opinion in Colloid & Interface Science, 2013. **18**(4): p. 311-323.
22. Cicuta, P. and A.M. Donald, *Microrheology: a review of the method and applications.* Soft Matter, 2007. **3**(12): p. 1449-1455.
23. MacKintosh, F.C. and C.F. Schmidt, *Microrheology.* Current Opinion in Colloid & Interface Science, 1999. **4**(4): p. 300-307.
24. Gisler, T. and D.A. Weitz, *Tracer microrheology in complex fluids.* Current Opinion in Colloid & Interface Science, 1998. **3**(6): p. 586-592.
25. Mason, T.G., et al., *Particle tracking microrheology of complex fluids.* Physical Review Letters, 1997. **79**(17): p. 3282-3285.
26. Waigh, T.A., *Microrheology of complex fluids.* Reports on Progress in Physics, 2005. **68**(3): p. 685-742.
27. Weihs, D., T.G. Mason, and M.A. Teitell, *Bio-microrheology: A frontier in microrheology.* Biophysical Journal, 2006. **91**(11): p. 4296-4305.
28. Leighton, D. and A. Acrivos, *MEASUREMENT OF SHEAR-INDUCED SELF-DIFFUSION IN CONCENTRATED SUSPENSIONS OF SPHERES.* Journal of Fluid Mechanics, 1987. **177**: p. 109-131.
29. Breedveld, V., et al., *Measurement of the full shear-induced self-diffusion tensor of noncolloidal suspensions.* Journal of Chemical Physics, 2002. **116**(23): p. 10529-10535.
30. Breedveld, V., et al., *Measuring shear-induced self-diffusion in a counterrotating geometry.* Physical Review E, 2001. **63**(2).
31. Xu, H.T., A.P. Reeves, and M.Y. Louge, *Measurement errors in the mean and fluctuation velocities of spherical grains from a computer analysis of digital images.* Review of Scientific Instruments, 2004. **75**(4): p. 811-819.
32. Breedveld, V., et al., *Shear-induced diffusion and rheology of noncolloidal suspensions: Time scales and particle displacements.* Journal of Chemical Physics, 2001. **114**(13): p. 5923-5936.
33. Besseling, R., et al., *Quantitative imaging of colloidal flows.* Advances in Colloid and Interface Science, 2009. **146**(1-2): p. 1-17.
34. Semwogerere, D. and E.R. Weeks, *Shear-induced particle migration in binary colloidal suspensions.* Physics of Fluids, 2008. **20**(4).
35. Crocker, J.C. and D.G. Grier, *Methods of digital video microscopy for colloidal studies.* Journal of Colloid and Interface Science, 1996. **179**(1): p. 298-310.
36. Ghosh, S., Mugele, F and Duits, MHG, *Effects of shear and walls on the diffusion of colloids in microchannels.* submitted, 2015.
37. Verhaegh, N.A.M. and A. Vanblaaderen, *DISPERSIONS OF RHODAMINE-LABELED SILICA SPHERES - SYNTHESIS, CHARACTERIZATION, AND FLUORESCENCE CONFOCAL SCANNING LASER MICROSCOPY.* Langmuir, 1994. **10**(5): p. 1427-1438.
38. Uricanu, V.I. and M.H.G. Duits, *Micromechanical behavior of adhesive granular silica layers: Structure deformation.* Langmuir, 2006. **22**: p. 7783-7792.
39. Weeks, E.R., http://www.physics.emory.edu/faculty/weeks//idl/.
40. Tolpekin, V.A., et al., *Aggregation and breakup of colloidal particle aggregates in shear flow, studied with video microscopy.* Langmuir, 2004. **20**(7): p. 2614-2627.
41. Savin, T. and P.S. Doyle, *Static and dynamic errors in particle tracking microrheology.* Biophysical Journal, 2005. **88**(1): p. 623-638.

42. Breedveld, V. and D.J. Pine, *Microrheology as a tool for high-throughput screening.* Journal of Materials Science, 2003. **38**(22): p. 4461-4470.
43. Besseling, R., et al., *Three-dimensional imaging of colloidal glasses under steady shear.* Physical Review Letters, 2007. **99**(2).
44. Kowalczyk, A., C. Oelschlaeger, and N. Willenbacher, *Tracking errors in 2D multiple particle tracking microrheology.* Measurement Science & Technology, 2015. **26**(1).
45. Bruus, H., *Theoretical Microfluidics* 1ed. 2008: Oxford University Press.
46. Dekruif, C.G., et al., *HARD-SPHERE COLLOIDAL DISPERSIONS - VISCOSITY AS A FUNCTION OF SHEAR RATE AND VOLUME FRACTION.* Journal of Chemical Physics, 1985. **83**(9): p. 4717-4725.
47. Eral, H.B., et al., *Anisotropic and Hindered Diffusion of Colloidal Particles in a Closed Cylinder.* Langmuir, 2010. **26**(22): p. 16722-16729.
48. Eral, H.B., F. Mugele, and M.H.G. Duits, *Colloidal Dynamics Near a Particle-Covered Surface.* Langmuir, 2011. **27**(20): p. 12297-12303.
49. Klein, S.A., et al., *Three-dimensional three-component particle velocimetry for microscale flows using volumetric scanning.* Measurement Science & Technology, 2012. **23**(8).